Bridging energy bands to the crystalline and amorphous states of Si QDs

Faraday Discussions

Accepted Manuscript

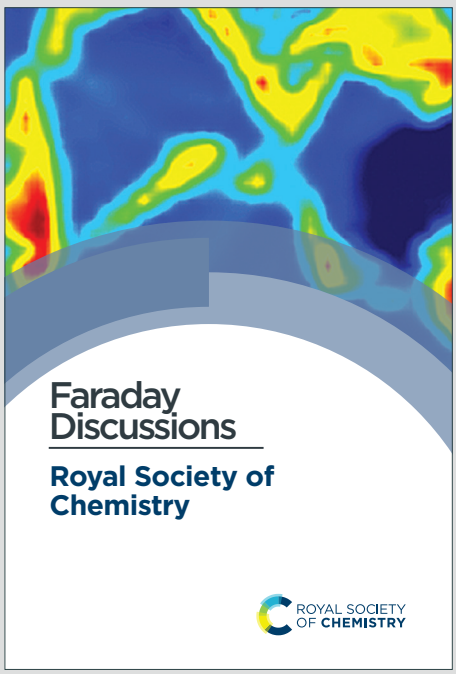

This article can be cited before page numbers have been issued, to do this please use: D. Mariotti, B. Alessi, M. Chiranjeevi, M. Macias-Montero, V. Svrcek and P. Maguire, *Faraday Discuss.*, 2020, DOI: 10.1039/C9FD00103D.

ROYAL SOCIETY OF CHEMISTRY

www.rsc.org/faraday_d

View Article Online
DOI: 10.1039/C9FD00103D

Bridging energy bands to the crystalline and amorphous states of Si QDs

Bruno Alessi[1*], *Manuel Macias-Montero*[2], *Chiranjeevi Maddi*[1], *Paul Maguire*[1], *Vladimir Svrcek*[3], *Davide Mariotti*[1]

[1]Nanotechnology and Integrated Bio-Engineering Centre (NIBEC), Ulster University, Newtownabbey BT37 0QB, United Kingdom

[2]Laser Processing Group, Institute of Optics (CSIC), Serrano 121, 28006 Madrid, Spain

[3]Research Center for Photovoltaics National Institute of Advanced Industrial Science and Technology (AIST) Central 2, Umezono 1–1–1, Tsukuba, 305–8568, Japan

[*]e-mail: alessi-b@ulster.ac.uk

Keywords

Silicon quantum dots, atmospheric-pressure plasmas, valence electron energy diagram, crystallization process

Abstract

The relationship between crystallization process and opto-electronic properties of silicon quantum dots (Si QDs) synthesized by atmospheric pressure plasmas (APPs) is studied in this work. The synthesis of Si QDs is carried out flowing silane as gas precursor in a plasma confined to a submillimeter space. Experimental conditions are adjusted to propitiate the crystallization of the Si QDs and produce QDs with both an amorphous and a crystalline character. In all the cases, Si QDs present a well-defined particle mean size in the range of 1.5-5.5 nm. Si QDs present optical bandgaps between 2.3 eV and 2.5 eV, which are affected by quantum confinement. Plasma parameters evaluated using optical emission spectroscopy are then used as inputs for a collisional plasma model, whose calculations yield the surface temperature of the Si QDs within the plasma, justifying the crystallization behavior for certain experimental conditions. We measure the ultraviolet-visible optical properties and electronic properties through various techniques, build an energy level diagram for the valence electrons region as a function of the crystallinity of the QDs and finally discuss the integration of these as active layers of all-inorganic solar cells.

1. Introduction

View Article Online
DOI: 10.1039/C9FD00103D

The unique properties of silicon quantum dots (QDs) have attracted great attention in numerous fields of science such as photonics, photovoltaics, electronics or biomedicine [1-5] for the unique interplay between quantum effects, surface states and direct/indirect transition dynamics and their biocompatibility [6-8]. Over the last decade, the focus has been on crystalline Si QDs [9-14], and the efforts made on the study of amorphous Si QDs have been very limited [15-18] due to the difficulty of preserving the individual character of the QDs. Nonetheless, both phases present distinguished and remarkable features. Amorphous silicon thin films often offer better transport properties due to enhanced structural disorder preventing radiative recombination [19] and tunability of their optical absorption edge by controlling hydrogen content [16]. At the nanoscale, QDs can provide added functionalities not available from bulk silicon for amorphous and crystalline Si, in combination with other nanoscale properties (surface-to-volume ratio, surface chemistries, etc.). The synthesis of Si QDs by low-pressure plasma has been the focus of extended research work that has revealed the benefits of plasma processes for nanomaterials synthesis [20-23]. Non-thermal plasmas at atmospheric pressure offer beneficial and complementary features but have received limited attention.

Atmospheric pressure plasmas (APPs) present great versatility for the production and treatment of nanomaterials [24, 25] for they allow flexible design and easy integrability. Also, at this pressure, ion collisions with the surface of nanoparticles are responsible for particle heating above the background gas temperature, allowing a controlled crystallization [14] by carefully tuning the synthesis conditions. We have previously studied the synthesis and materials properties of crystalline and amorphous silicon QDs, separately, by atmospheric pressure plasmas (APPs) [16, 26, 27]. Our approach produced Si QDs with well-defined particle size and with observable quantum confinement effects.

Herein, we present an experimental and theoretical investigation of the Si QDs phase transition in APPs, comparing the plasma conditions leading to or preventing crystallization.

We then perform various measurements on selected samples to assess the energy band diagrams and derive the relationships between structural features and opto-electronic properties in function of synthesis conditions. In this context we use different measurements techniques to build an energy level diagram of near-gap electron states, and critically compare methods and results. This approach is important for implementing nanomaterials in real world applications.

Finally, we test the applicability of our Si QDs integrating them as active layers in all-inorganic solar cells. While these devices still present very low efficiencies, here we demonstrate the viability of APP processes to be used in the manufacturing of next generation photovoltaics.

2. Experimental details

View Article Online
DOI: 10.1039/C9FD00103D

The plasma reactor used for the synthesis of Si QDs operates in a parallel electrode configuration at atmospheric pressure (760 Torr). A schematic diagram of the system is depicted in Figure S1 of supporting information. The plasma is generated inside a rectangular glass tube with a 0.5 mm gap and 0.3 mm of wall thickness. Radio frequency (RF) power at 13.56 MHz and 120 W is applied through a matching unit and to two rectangular copper electrodes with a section of 20 mm x 5 mm.

Argon and hydrogen are supplied as background gases, while silane (SiH_4) is used as Si precursor varying its concentration between 50 ppm and 200 ppm. The flows of Ar and H_2 are set to 810-840 sccm and 150 sccm respectively, in order to keep concentrations of 99.7% and 0.3% approximately at a fixed total flow of 1 sLm. The plasma setup is accessorized with a two-axis stage and it is possible to directly deposit Si QDs on a substrate and form homogeneous films [26]. The plasma conditions are characterized using optical emission spectroscopy. The equipment used to acquire the emission spectra is an Ocean Optics HR4000CG UV-NIR spectrometer (range 194-1122 nm) coupled with a 50 μm optic fiber. These measurements are carried out locating one end of the optic fiber perpendicular to the plasma 10 mm away.

Silicon QDs are characterized using transmission electron microscopy (TEM) with a JEOL JEM-2100F microscope. The TEM analysis includes bright-field imaging to observe the morphology of the QDs and selected area electron diffraction (SAED) to characterize their crystallinity. For TEM, the QDs are collected directly in vials containing ethanol and then drop casted onto an ultrathin carbon grid (Agar Scientific). Chemical analysis is performed using Fourier transform infrared spectroscopy (FTIR) and X-ray photoelectron spectroscopy (XPS) core levels measurements. The FTIR is a Nicolet iS5 from Thermo Scientific equipped with an attenuated total reflectance (ATR) iD5 accessory. XPS and ultraviolet photoelectron spectroscopy (UPS) measurements were performed using an ESCALAB 250 Xi microprobe spectrometer (Thermo Fisher Scientific, UK), equipped with an X-ray and UV source. XPS analysis was carried out with a focused XR6 monochromatic, micro-focused $Al_{K\alpha}$ (hν=1486.6 eV, <900 μm spot sizes) radiation source with a hemispherical energy analyzer. The binding energy was calibrated against the Pt_{4f} peak taken to be located at 72.1 eV with a pass energy of 150 eV. XPS measurements were carried at a pressure 1-5 $\times 10^{-9}$ mbar. The valence band spectra were collected with a 20 eV pass energy. Optical absorption is obtained using a Perkin-Elmer 650S ultraviolet-visible (UV-Vis) spectrometer equipped with a 150 mm integrating sphere. For UV-Vis characterization, Si QDs were deposited on a quartz substrate forming a homogeneous film. For valence electron analysis XPS in the valence region, UPS and a Kelvin Probe were used. UPS spectra were collected with a UV source energy He(I) ($h\nu = 21.22$ eV) at a pressure of approximately 5.5 $\times$ 10^{-8} mbar, with 2 eV pass energy. A negative bias of 10 V was applied to the sample to shift the

spectra from the spectrometer threshold. The energy resolution was around ~100 meV. The Kelvin probe (KP technologies APS04) is operated in atmosphere with a 2 mm gold alloy tip, after calibrating the tip work function against a sputtered Au thin film ($W_{Au} = 4.69 \pm 0.05$ eV, $W_{tip} = 4.4 \pm 0.1$ eV). Additionally, the Kelvin probe (KP) setup is equipped with a surface photovoltage module which measures the surface contact potential difference (CPD) induced by a monochromated white light source and an air photoemission module (APS), which uses a deuterium lamp source ($\Delta\lambda$=1 nm) to induce photoemission of electrons from the samples. For XPS, UPS and KP samples are directly deposited to form a film of QDs on an ITO-coated glass (150 nm, 15 Ω/sq. VisionTek) in order to have good electrical contact with the stubs. The characterization of all the samples was carried out within 1 hour after the synthesis to limit the effect oxidation [26].

3. Results and Discussion

3.1 Structural and chemical characterization

TEM results show that well-separated Si particles are produced for all values of precursor concentration introduced into the plasma (Figure S1 in supporting information). However, high resolution TEM (HR-TEM) images reveal major differences between the particles depending on the precursor concentration. In particular, high silane concentrations (150-200 ppm) lead to the production of amorphous particles, while with low concentrations (50 ppm) crystalline particles are obtained (Figure 1). As an example, figure 1a-b displays HR-TEM of a crystalline QD synthesized using a SiH_4 concentration of 50 ppm and an amorphous QD produced with 200 ppm of the precursor, respectively. In Figure 1a, the particle exhibits fringes with spacing of 0.17 nm that corresponds to the (311) plane of the silicon crystalline lattice. More detailed evidence of the crystalline or amorphous character of the Si QDs is obtained using SAED. Figure 1c-d show SAED patterns for the two extreme conditions of precursor concentration considered (50 ppm and 200 ppm). The crystallinity of the Si QDs produced using low SiH_4 concentration, results in the observation of sharp spots that together form well-defined rings in the SAED pattern (figure 1c). The spots detected in the diffractogram match well with crystalline planes corresponding to the diamond lattice of silicon (see Figure S2 of the supporting information). On the other hand, a high concentration of precursor (150-200 ppm) results in faded diffuse rings in the SAED pattern that can be attributed to their amorphous character (Figure 1d). The conditions described above illustrate how our APP system is capable of producing highly crystalline QDs or purely amorphous QDs by controlling, in this case, the silicon precursor concentration. These results are in agreement with previous results published elsewhere [14, 16]. Hence, it is possible to adjust from crystalline Si QDs production with low precursor concentration in the plasma (≤ 50 ppm),

to amorphous Si QDs with high concentrations (≥ 150 ppm). For intermediate conditions the situation exhibits significant differences. TEM analysis of samples prepared using 100 ppm of SiH_4 concentration showed that within the particle size distribution, only the smallest (< 2 nm) particles exhibited crystalline character, while larger particles were amorphous. Thus, at these conditions both crystalline and amorphous particles can be generated simultaneously. To further understand the mechanism that makes possible the crystallization process of QDs inside the plasma region, a collision-corrected model (CCM) has been used and the results are described below. Regarding the particle size analysis, low magnification TEM images have been used, counting over 500 QDs for each of the conditions. The TEM micrographs used for the calculations and the particle size histograms are included in figure S3 of the supporting information. The overall results are presented in figure 1e, showing the mean value and the standard deviation (these were obtained by fitting a log-normal distribution) of the QD size for various precursor concentrations, indicating the crystalline or amorphous character with red and blue color respectively. In the graph it is possible to observe that increasing the concentration of precursor in the plasma leads to the production of QDs with larger in size, with mean diameters varying from 1.7 nm to 3.6 nm. At the same time, the size dispersion also increases starting with a value of 0.6 nm for 50 ppm of SiH_4 and reaching a value of 1.8 nm for 200 ppm of SiH_4.

XPS technique has been used to characterize chemically the Si QDs produced for the different experimental conditions. The photoelectron spectra in the Si 2p region are shown in Figure 2a, along with a deconvolution of the peaks in the different oxidation states of Si. We can observe that only the crystalline samples show a higher binding energy shoulder which can be readily associated with limited oxidation. On the contrary, samples which have a least a fraction of amorphous particles do not show this feature.

Further details on the chemical composition of the Si QDs were produced by FTIR analysis. Figure 2b displays the FTIR spectra of Si QDs produced using the indicated SiH_4 concentration in the plasma. In the two selected regions of the infrared spectrum shown in figure 2b, it is possible to observe the vibrations that correspond to Si-O and Si-H_x bonds. In particular, the absorption band at ~1075 cm^{-1} associated to Si-O-Si stretching modes is shown. This peak has very strong absorption cross section and therefore the low absorbance (lower than the Si-H_x peaks) is evidence of a small level of oxidation even after exposure to atmosphere. Instead, the peaks at 783 cm^{-1}, 862 cm^{-1}, 902 cm^{-1} and 2139 cm^{-1} are associated with the Si-H_3 bending, symmetric deformation, degenerate deformation and stretching mode, respectively [28,29]. The intensity of these peaks becomes significant for Si QDs synthesized using high precursor concentration (200 ppm) which correspond to amorphous samples, while it is negligible for lower concentrations when particles are crystalline. This suggests that when the synthesis is carried out using a silane concentration above 100 ppm, i.e. whenever some amorphous material is present, particles become partially hydrogenated possibly due to hydrogen incorporation within the QDs [16].

View Article Online
DOI: 10.1039/C9FD00103D

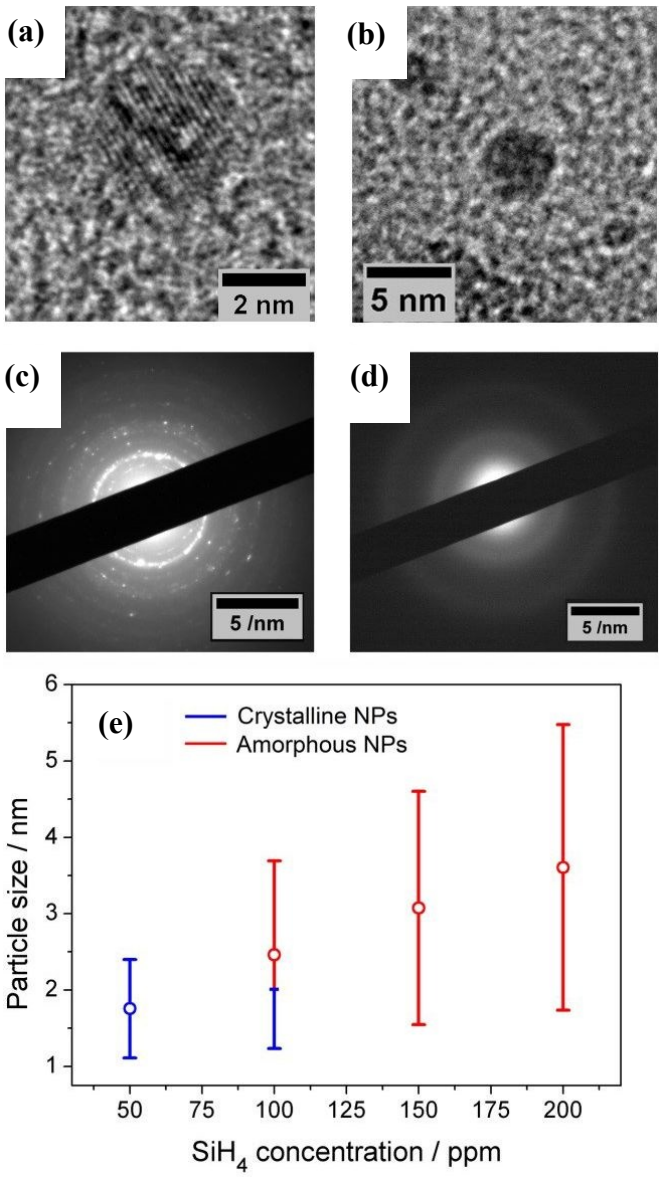

Figure 1. *Transmission electron microscopy (TEM) characterization of the Si quantum dots (QDs). High resolution TEM of* ***(a)*** *a crystalline and* ***(b)*** *amorphous Si QD.* ***(c) – (d)*** *Selected area electron diffraction (SAED) pattern of a) crystalline and b) amorphous Si QDs.* ***(e)*** *Mean particle size (dots) and standard deviation (bars) of the Si QDs as a function of the precursor concentration used; blue and red lines denote respectively the crystalline or amorphous character of the QDs within the size distribution.*

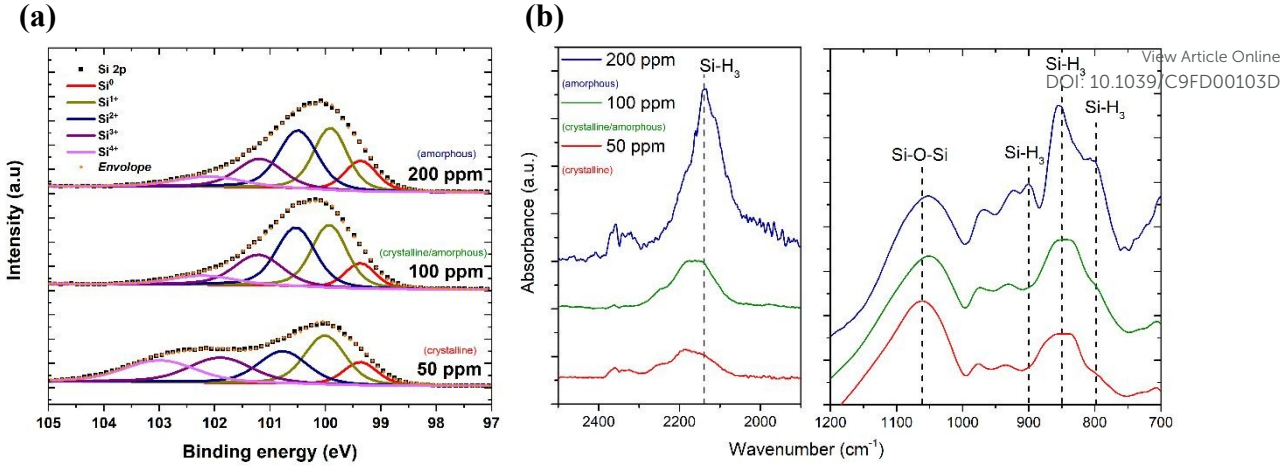

Figure 2 – (a) *Deconvolution of XPS Si2p signal into components relative to the different oxidation state of Si atoms, reflecting and increased amount of Si-O bonds with different coordinations for the sample with crystalline nanoparticles.* ***(b)*** *Fourier transform infrared (FTIR) spectra of Si QDs for the different precursor concentrations indicated. The dashed line indicates vibrational transitions at 783 cm^{-1}, 862 cm^{-1}, 902 cm^{-1} and 2139 cm^{-1} wavenumbers and are associated with the Si-H_3 bending, symmetric deformation, degenerate deformation and stretching mode, respectively and a Si-O-Si absorption band at 1075 cm^{-1} .*

We already reported the stability of Si nanocrystals through FTIR measurements in a previous study [26] over a period of 30 days and concluded that these nanocrystals, while being H-terminated, tend to oxidize through a backbond oxidation process starting from water (e.g. from humidity in air) condensation on the surface. However, this process is slow and self-limited particularly when the QDs are deposited in films. Interestingly the amorphous particles seem to be protected from oxidation at least in the first stages of exposure to atmosphere (<1 h) and within the volume scoped by the XPS, a fact that could be ascribed to the different kinetics of oxidation within amorphous particles [30,31] or due to the higher H concentration and the ability of hydrogen to passivate dangling bonds more evenly than in the crystalline case. The degree of hydrogenation therefore seems to be important both in the oxidation process as well as at some level determining the phase of the QDs.

The XPS instrument also allows the acquisition of reflection electron energy loss spectra using the flood gun as an electron source. This technique can be used to easily ascertain qualitatively the presence of incorporated hydrogen within a sample, via an energy loss feature which sits around 1.8 eV from the zero-loss peak. In our case we observe a (Figure S4, supporting information) distinguishable peak for the conditions in which we obtain amorphous particles (100 ppm and 200 ppm) of SiH_4. We believe that at these conditions the level of hydrogenation is higher than in the other cases. When the QDs are crystalline (50 ppm) the presence of hydrogen is limited at the surface and for this reason the hydrogen reflection signal is essentially absent.

3.2 Formation mechanisms leading to the synthesis of Si QDs

We used a model to calculate the temperature at the surface of the Si QDs (T_p) during the synthesis process within the APP (see section S6 in Supporting Information). Figure 3 presents the estimated values of T_p corresponding to our synthesis conditions (black, red, green and blue squares); in the same graph we also plot the experimental crystallization temperature (CT, grey points) of Si QDs from the literature [32]. The CT divides the graph in two regions: particles with a temperature below the CT are expected to be amorphous (blue region in figure 3) while particles with a temperature above the CT are expected to present a crystalline character (orange region in Figure 3). Due to the intrinsic difficulty for measuring these values, it is not possible to define a sharp CT line to separate the two states [32]. Instead, a transition region represented by a white band can be defined (see Figure 3). It is possible to observe that for low SiH_4 concentrations (50 ppm, black squares) the data points are all located entirely on the crystalline side of the graph. This result clearly agrees with the experimental evidence reported in figure 1, that is, the formation of purely crystalline Si QDs. For high precursor concentrations (> 100 ppm) the opposite situation is observed. In this case, T_p is mainly located in the amorphous region with only the smallest, and less numerous, particles near the crystallization band. This is again in agreement with experimental data of Figure 1, where amorphous particles were observed for these conditions. The inability to produce a sufficiently high QD temperature for the crystallization of the Si QDs under these conditions can be partly attributed to the lower energetic plasma conditions (see Figure S5) but also to the larger particle size produced. At intermediate SiH_4 flow (100 ppm), only the smallest particles are located on the crystalline side and the rest lay on the crystallization band as indeed confirmed in our QDs characterization (Figure 1). These results provide theoretical justification to the experimental observations since only particles smaller than 2 nm were found to be crystalline for this intermediate condition.

3.3 Valence band, Fermi level and bandgap measurements

The functional properties of semiconductors, in particular for energy applications, depend on the electronic structure and how the energy band parameters align with other application device components. We therefore perform here the experimental evaluation of energy band diagram (EBD) parameters such as valence/conduction band edges, Fermi level and bandgap for our samples. All measurements are therefore conducted on films of QDs deposited on solid substrates. Firstly, we focus on the valence band maximum (VBM) and Fermi level; in the next section we will complement these results with bandgap measurements to produce the EBD of both crystalline and amorphous QDs. To evaluate the electron energy levels near the valence band region and Fermi levels, we combined and compared results from different measurement techniques which offer different features, whose results are reported in Table 1.

View Article Online
DOI: 10.1039/C9FD00103D

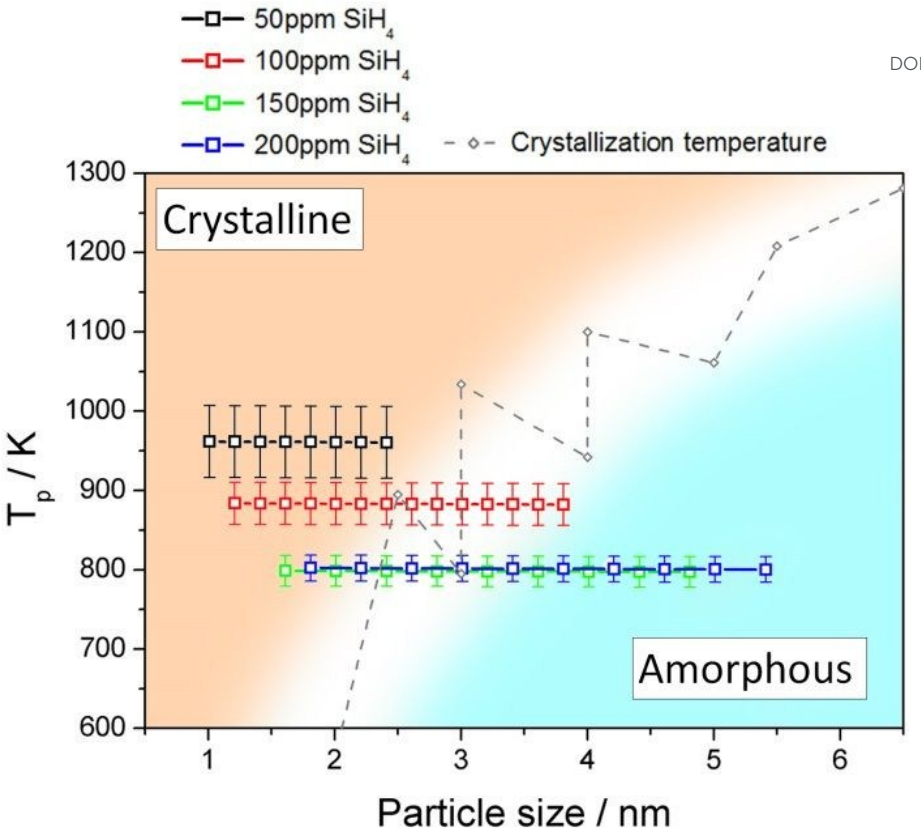

243 ***Figure 3.*** *Particle temperature calculated using the collision-corrected model (CCM) for the*
244 *different concentration of precursor introduced in the plasma and experimental crystallization*
245 *temperature from reference [32]. The temperature has been calculated for the particle size*
246 *distribution obtained for each condition. The crystallization temperature divides the graph in*
247 *crystalline (orange) and amorphous (blue) regions.*

248

	Fermi Level / eV		VBM / eV			Eg / eV
Sample	$E_{F\text{-}Kp}$	$E_{F\text{-}UPS}$	VBM_{UPS}	VBM_{XPS}	VBM_{APS}	$E_{g\text{-}UVVIS}$
50 ppm	- 6.0 ±0.1	- 4.7 ±0.1	-5.9 ±0.1	-6.3 ±0.6	-5.7 ±0.2	2.47 ±0.07
100 ppm	- 4.0 ±0.1	- 4.3 ±0.1	-6.2 ±0.1	-6.4 ±0.6	-6.1 ±0.2	2.6 ±0.1
200 ppm	- 3.9 ±0.1	- 3.5 ±0.1	-5.7 ±0.1	-5.8 ±0.6	-5.8 ± 0.3	2.3 ±0.1

249

250 ***Table 1*** *- Fermi levels determined from Kelvin probe ($E_{F\text{-}Kp}$) and UPS ($E_{F\text{-}UPS}$) measurements with*
251 *corresponding errors. For the Kelvin probe measurement, the error corresponds to std. deviation*
252 *measurements within the scoped area and for the UPS measurement it is mostly due to the*
253 *spectrometer energy resolution. VBM values determined from UPS (VBM_{UPS}) and APS (VBM_{APS})*
254 *with corresponding errors are also reported. VBM_{XPS} was calculated from XPS measurements*
255 *and the Fermi levels produced by UPS. Errors correspond to energy resolution for UPS and XPS,*
256 *and for APS a rms sum of std. deviation relative to the fit. Energy bandgaps obtained through*
257 *Tauc plots of transmittance and reflectance measurements, assuming an indirect bandgap*
258 *functional dependence between absorption coefficient and light energy. Errors are a rms sum of*
259 *errors from fitting and uncertainty due to the light source instabilities.*

UPS can be used to obtain the absolute value of the Fermi Level of a semiconductor as well as the VBM. UPS measurements produce a cut-off energy ($E_{cut\text{-}off}$) and an on-set energy ($E_{on\text{-}set}$) which relate to the binding energy of electrons originating from the deepest levels of the material (ionized by the He-I source, $hv = 21.22$ eV) and from the valence band region, respectively (Figure 4a). We should note that the UPS signal is referenced to the Fermi level of the semiconductor material under analysis. Therefore, the Fermi level can be extracted from the difference between $E_{cut\text{-}off}$ and the energy of the He-I photons, i.e. $E_{F\text{-}UPS} = E_{cut\text{-}off}$ - 21.22 eV (see Table 1). The VBM is calculated also from the UPS measurements where $VBM_{UPS} = E_{F\text{-}UPS} - E_{on\text{-}set}$ (Table 1).

Fermi level values obtained with the Kelvin Probe show the same trend as the ones obtained by UPS, even though the values are different, and in one case (50 ppm) particularly higher.

Meanwhile XPS produces the difference between the Fermi level and the VBM (Figure 4b). In order to determine the values of the VBM reported in Table 1, we have used the Fermi levels obtained by UPS (also in Table 1). Finally, the APS technique is similar in principle to the lower energy range of the UPS, but it is operated in atmosphere and the source is a deuterium lamp, which is not able to reach a cut-off in the photoemitted electrons. From the APS signal it is possible to extract an absolute value of VBM (See supporting information section S9).

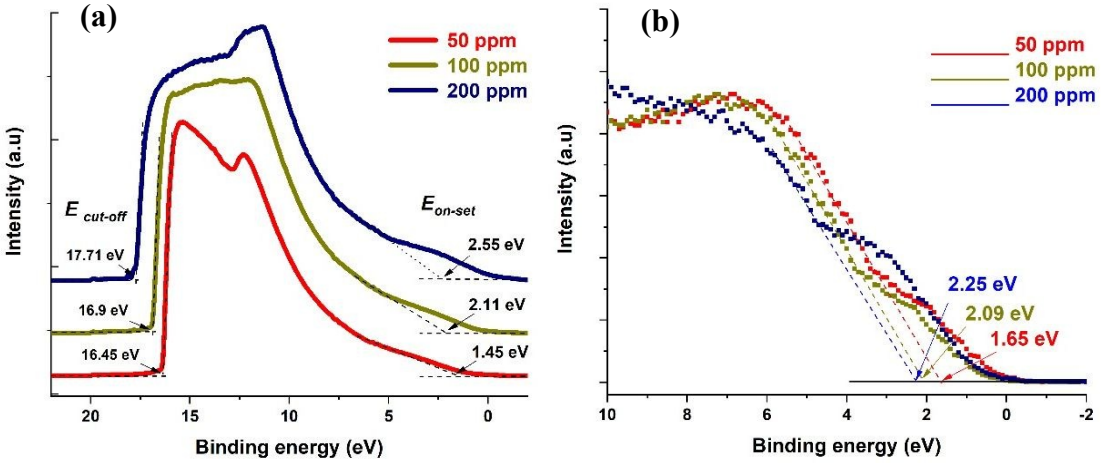

Figure 4 *– **(a)** UPS spectra for the three different samples showing both cut-off and on-set values. **(b)** XPS valence band spectra showing the difference between VBM and Fermi level.*

All the values summarized in Table 1 are also reported in Figure 5. The comparison shows that discrepancies from different measurements do exist, which in most cases are within measurement errors. Differences even above 0.1 eV can be significant for applications, however we should note that the literature seldomly reports a comparison of different measurement techniques and as such our results highlight and underline the difficulties and limitations of current and available measurement methods.

With the exception for one of the measurements, the Fermi levels show similar values and exhibit the same trend, i.e. the Fermi energy becoming smaller with the particles going from crystalline to amorphous (Figure 5a). The value of the Fermi level for the crystalline QDs (50 ppm) stands out and emphasizes the strong surface sensitivity of the KP technique (1-3 monolayers); while stray capacitance originating from inhomogeneities in the film can also impact the measurement, we tentatively ascribe this very large value of the Fermi level to the impact of even minor surface oxidation. The VBM values also show similar trends (Figure 5b) with differences that can be justified by measurement errors, with the exception of the VBM values of crystalline QDs (50 ppm) measured by XPS, which may be due to difficulties in extracting a good and reliable fit to the x-axis due to the limited resolution. A critical evaluation of the capabilities of each technique is therefore needed in order to choose which approach is most suitable and reliable in this specific case.

UPS measurements are implicitly limited by the general mechanism involved in the photoemission as the light interacting with the sample induces a surface dipole which complicate the evaluation of the Fermi level and VBM values, especially in conductive or highly doped samples [33]. In our case we assume that our samples are not developing a particularly strong surface dipole, since we do not expect the samples to be highly conductive. However, the UPS signal strength rely on the high photoemission yield, the narrow energy resolution achievable and the ability to scope only the occupied electron states of the very top surface of a solid (2-3 nm). Instead XPS in the valence band region suffers from moderate energy resolution, lower yields and the absence of an energy cut-off which does not permit to obtain values relative to the vacuum level and generally scopes a “deeper” region beneath the surface (5-10 nm) [34]. Both techniques though are operated in high vacuum, which can help preserving the state of surfaces.

KP and associated APS operated in atmosphere are instead subject to surface dipoles and surface chemistry induced by environmental adsorbates which can easily shift the values up to few eV raising or lowering the barriers felt by electrons escaping the material or even induce completely new energy levels, especially in the valence electrons region. These may be considered as systematic errors in the values, which cannot be accounted for if there is not a rigorous knowledge of the surface chemistry. While they are mostly useful for characterizing surfaces which will be exposed to atmosphere (e.g. for corrosion studies) they also have advantages of being cheap, easy and fast techniques. In addition, KP measurements are not affected by light-induced dipoles. However, APS operates in atmosphere and photoelectrons experience different electrostatic environment as higher or lower potential barriers when escaping from the material’s surface.

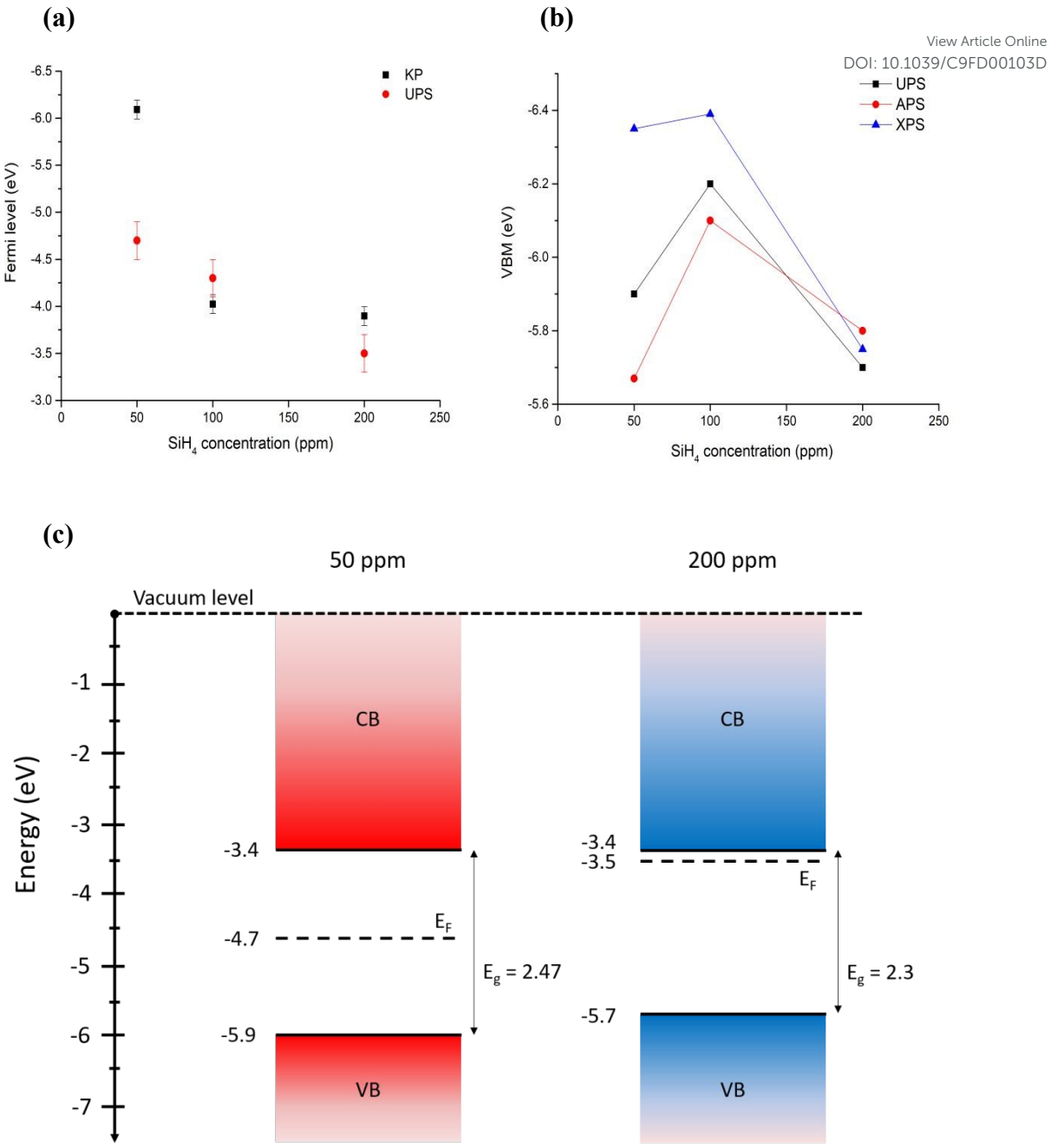

Figure 5 – (a) *Comparison of Fermi level measured with Kelvin Probe and UPS.* ***(b)*** *Comparison of VBM values measured (UPS, APS) and calculated (XPS) with different techniques, error bars are omitted for clarity and can be found in table 1.* ***(c)*** *Energy band diagrams obtained combining UPS values for Fermi level and VBM, and energy bandgaps through Tauc plots for the extreme cases 50 ppm and 200 ppm of Silane, which correspond to the smallest (<r>=1.8 nm) all crystalline particles and the biggest (<r>=3.6 nm) all-amorphous ones.*

These conditions depend on the atmospheric species and can change substantially with ambient temperature and humidity. In other words, while UPS and XPS are referenced to a potential energy of the ultra-high vacuum in the XPS chamber, the APS values are referenced to the

electrostatic potential at the atmospheric conditions at the time of measurements [35]. It is clear that various techniques can be used for the determination of VBM and Fermi levels, however care should be taken in the selection of the most appropriate technique.

UV-Vis transmission and reflectance spectra were acquired for Si QDs. In all the cases, Si QDs exhibit continuous and relatively featureless optical characteristics. Transmission and reflectance measurements can be used to determine the bandgap of the Si QDs. A full description of the bandgap determination can be found in the supporting information (section S7), which were calculated using Tauc plots with a 1/2 coefficient corresponding to an indirect bandgap [36]. A similar argument holds for amorphous silicon particles, for which the joint optical density of states is modeled by a square law [37,38]. For low precursor concentrations (50 ppm), QDs present a bandgap of roughly 2.5 eV (see Table 1) and as previously observed (Figure 1e) these experimental conditions generate crystalline particles. This value is consistent with H-terminated Si-QDs in the size range reported (1.8 nm). However, for SiH_4 concentrations greater than 100 ppm, value at which we start to observe amorphous particles (Figure 1e), the bandgap (more rigorously mobility gap) tends to a value of about 2.3-2.5 eV, which is consistent with the expected value for amorphous Si [39]. The bulk bandgap of amorphous silicon is reported in the wide range 1.6-1.97 eV, a condition that strongly depends on the content of hydrogen and on the degree of structural disorder introducing or relieving stress components. The relative importance of the two mechanisms is still debated [40-42]. The higher values in respect to bulk counterparts may be ascribed to quantum confinement effects, given the small particle size that we obtained. This fact could be explained by an increased content of hydrogen which has been found with the REELS spectrum (Figure S4 in supporting information). The 200 ppm Silane samples, which resulted in the biggest amorphous-only particles, additionally shows a long absorption tail to sub-bandgap energies that may be due to unsaturated bonds, ultimately acting as shallow dopant levels.

The surface photovoltage module in the KP can detect small amounts of photoinduced charge on a sample surface. The ability to build charge on the surface depends both on the light-induced bending of energy levels due to surface states, that results either in charge accumulation or depletion, and charge carriers mobilities [43]. We observe a detectable photovoltage only in the samples with amorphous particles (see Figure S8 in supporting information). The threshold in energy for the appearance of a photovoltage shows similar values as optical gaps (2.3 eV to 2.5 eV) found via UV-Vis absorption, and the sign of the shift indicates that samples have an n-type behavior. This implies that charge transport within the layer of amorphous particles may be superior in respect to the films of crystalline nanoparticles [43].

3.3 Energy level diagram

Based on our discussion in section 3.2, we can expect XPS and APS to be somewhat less accurate for the determination of the VBM. The former because of a lower counts and resolution at lower energies which tend to overestimate the difference between VBM and Fermi level, given the inability to resolve weaker signals. The latter is susceptible to environmental conditions and adsorbates at a higher degree than the other techniques. For the same reason, Fermi level through Kelvin Probe may be equally dependent on the calibration value, which is obtained by the APS method and may be affected by ambient temperature, humidity and by adsorbates on the particle's surface.

We believe in conclusion that UPS values are more reliable both for the determination of absolute Fermi level and for the VBM, under the only assumption of negligible light-induced surface dipole. Using energy bandgap values from UV-Vis spectroscopy and UPS values, we have produced the energy band diagram of our single-phase samples (Figure 5c).

The result is that, while valence band maxima and bandgap do not vary significantly with the crystalline state of our nanoparticles, the value of Fermi level tend to get closer to the conduction band edge with increased amounts of amorphous particles giving a stronger n-type character to the films. The UV-Vis longer wavelength (sub-gap) absorption and the photovoltage response of amorphous samples do support this picture.

4. Application as active layers in PV cells

In this section we finally provide some details on the integration of Si QDs in photovoltaic (PV) devices. This is mainly to show that a better knowledge of the EBD parameters can benefit the application development and also in part to demonstrate the capability of the APP process for direct integration of QDs in experimental devices. We have evaluated the performance of all-inorganic PV cells using the crystalline Si QDs synthesized with our method (50 ppm). The particles are directly deposited as a homogeneous film with the help of a two-axis stage placed 1 cm below the exit orifice of the capillary. Two device architectures were explored, both having Si QDs as the active component for the photogeneration of electron-hole pairs (see also Supporting Information).

One of the device architectures is illustrated in figure 6a, the other in supporting information S10. We used indium-doped tin oxide (ITO) strip-coated glass (VisionTek Systems Ltd., 15 Ω/sq, 150 nm ITO thickness) as our substrate and transparent conductive contact. A TiO_2 layer (40 nm thick) is formed using a sol-gel method and spin-coating following the protocol previously described [44] on top of the transparent conductive substrate. The TiO_2 coated ITO-glass is then used as a substrate to directly deposit the Si QDs (3 μm thick film) exiting from the plasma reactor, using an X-Y stage to ameliorate the uniformity of the deposited layer. Spray-deposited Cu_2O is then used as an electron blocking layer and a sputter-deposited gold film is used as a top contact.

The non-equilibrated band diagram of the cell is shown in figure 6. We should note that the selection of the Cu_2O transport layer was informed from our EBD measurements. The performance of the device was assessed with a solar simulator (Sub Femtoamp Keithley 6430) at standard AM1.5 irradiation. Open-circuit voltage and fill factor of 0.785 V and 87% were obtained, respectively. These are remarkable figures of merit that we can partly ascribe to exceptional good energy level alignment of the Si QDs with the selected transport layer and contacts; however, the current density is very poor and is affecting the overall performance. Additionally, the measured value of series resistance is also indicative of relatively efficient electron transport in the cell (table S10 in supporting information). Our current set-up could not deliver thinner Si QDs films as normally employed in this type of devices; a reduction of the thickness can contribute to some improvements in the current density and overall device performance.

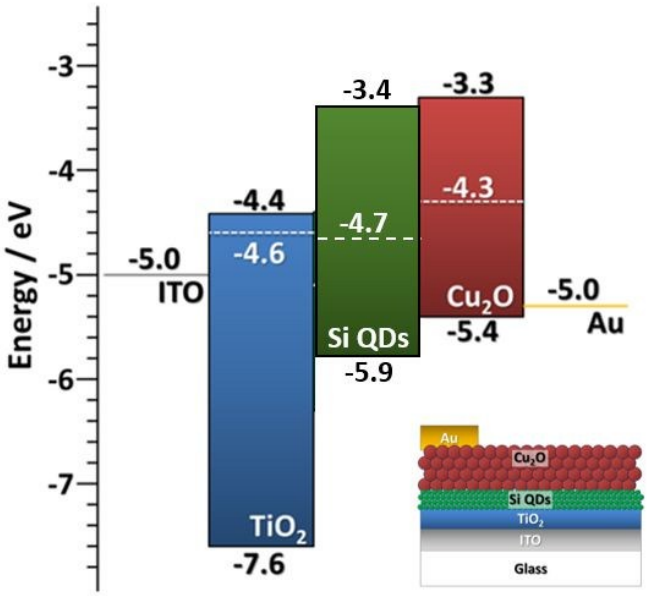

Figure 6. *Non-equilibrated band diagram for the PV device based on Si QDs as active layers, Cu_2O QDs as electron blocking layer, a TiO_2 film hole blocking layer and corresponding contacts. Inset, diagram of the layer structure of the relative device.*

While the overall performance remains very low, the device parameters are very encouraging and demonstrate the usefulness of a careful EBD parameters analysis. The utilization of both amorphous and crystalline Si QDs for PVs remains debatable and recent trends show that further manipulation through surface modification, alloying or other methodologies will be required [45,46]. In this context, the feasibility and integration of APP processes in the fabrication of next generation devices is very promising and can result advantageous.

View Article Online
DOI: 10.1039/C9FD00103D

5. Conclusions

We have demonstrated that Si QDs with tunable crystallinity can be grown in APPs. The study of a variety of experimental conditions has enabled us to produce Si QDs exhibiting crystalline or amorphous characteristics. The crystalline or amorphous character of the Si QDs was explained by the efficient heating of the particles in non-thermal APPs. The analysis of the energy balance on the surface of the particles shows that the plasma parameters can be tuned to control the temperature of the particles when immersed in the plasma and hence, their crystallinity. We built an electron energy diagram of the valence electrons regions for two selected samples, one with completely crystalline nanoparticles and one with completely amorphous nanoparticles and, after a critical assessment of measurements from different instruments, found that films formed from these free-standing particles tend to develop an n-type character for charge carrier in amorphous nanoparticles, despite similar values of valence band edges and optical bandgaps. We also showed the potential of APP processes for the fabrication of all-inorganic PV cells. Our analysis also highlights the need for improving analytical techniques and methodologies so that could be used more extensively to dictate application-focused research directions.

Acknowledgements

This work was supported by the EPSRC (EP/K022237/1, EP/M024938/1, EP/R008841/1) and the Leverhulme International Network (IN-2012-136).

References

[1] Priolo F, Gregorkiewicz T, Galli M and Krauss TF 2014 *Nat. Nanotechnol.* **9**, 19-32

[2] Mastronardi ML, Henderson EJ, Puzzo DP and Ozin GA 2012 *Adv. Mater.* **24**, 5890-5898

[3] Kim DK, Lai Y, Diroll BT, Murray CB and Kagan CR 2012 *Nat. Commun.* **3**, 1216

[4] Park J, Gu L, von Maltzahn G, Ruoslahti E, Bhatia SN and Sailor MJ 2009 *Nat. Mater.* **8**, 331-336

[5] Švrček V, Mariotti D, Shibata Y and Kondo M 2010 *J. Phys. D: Appl. Phys.* **43**, 415402-415410

[6] Mariotti D, Mitra S and Švrček V 2013 *Nanoscale* **5**, 1385-1398

[7] Švrček V, Kondo M, Kalia K and Mariotti D 2009 *Chem. Phys. Lett.* **478**, 224-229.

[8] Švrček V, Mariotti D and Kondo M 2010 *Appl. Phys. Lett.* **97**, 161502

[9] Wolf O Dasog M, Yang Z, Balberg I, Veinot JGC and Millo O 2013 *Nano Lett.* **13**, 2516-2521

[10] Dasog M, De los Reyes GB, Titova LV, Hegmann FA and Veinot JGC 2014 *ACS Nano* **8**, 9636-9648.

[11] Kusova K *et al* 2010 *ACS Nano* **4**, 4495-4502

[12] Švrček V, Dohnalova K, Mariotti D, Trinh MT, Limpens R, Mitra S, Gregorkiewicz T, Matsubara K and Kondo M 2013 *Adv. Funct. Mater.* **23**, 6051-6058

[13] Sagar DM, Atkin JM, Palomaki PKB, Neale NR, Blackburn JL, Johnson JC, Nozik AJ, Raschke MB and Beard MC 2015 *Nano Lett.* **15**, 1511-1516

[14] Askari S, Levchenko I, Ostrikov K, Maguire KP and Mariotti D 2014 *Appl. Phys. Lett.* **104**, 163103

[15] Askari S, Macias-Montero M, Velusamy T, Maguire P, Svrcek V and Mariotti D, 2015, *J. Phys. D: Appl. Phys.* **48**, 314002

[16] Askari S, Svrcek V, Maguire P and Mariotti D, 2015, *Adv. Mater.*, **27**, 8011–8016

[17] Anthony R and Kortshagen U, 2009, *Phys. Rev. B* **80**, 115407

[18] Shen Z, Kortshagen U, and Campbell SA, 2004, *J. Appl. Phys.* **96**, 2204

[19] Street RA 1981 *Adv. Phys.* **30**, 593-676

[20] Kortshagen U, 2009, *J. Phys. D: Appl. Phys*. **42** 113001

[21] Kortshagen U, Mangolini L, Bapat A, 2006 *Nanotechnology and Occupational Health*, 39-52

[22] Mangolini L, Thimsen E, and Kortshagen U, 2005, *Nano Lett.*, **5** (4), pp 655–659

[23] Gresback R, Holman Z, and Kortshagen U, 2007, *Appl. Phys. Lett.* **91**, 093119

[24] Mariotti, D.; Sankaran, R. M. Perspectives on atmospheric-pressure plasmas for nanofabrication, 2011 *J. Phys. D: Appl. Phys.*, **44**, 174023

[25] Wagner AJ, Mariotti D, Yurchenko KJ and Das TK 2009 *Phys. Rev. E* **80**, 065401.

[26] Macias-Montero M, Askari S, Mitra S, Rocks C, Ni C, Svrcek V, Connor PA, Maguire P, Irvine JTS and Mariotti D. 2016 *Nanoscale* **8**, 6623-6628

[27] Askari S, Macias-Montero M, Velusamy T, Maguire P, Svrcek V and Mariotti D, 2015*, J. Phys. D: Appl. Phys*. **48**, 314002

[28] Tautz F.S and Schaefer JA 1998 *J. Appl. Phys.* **84**, 6636-6643.

[29] Chabal YJ 1991 *Physica B* **170**, 447-456

[30] Z.H. Lu, E. Sacher and A. Yelo, 1988 Philosophical Magazine B

[31] A. Szekeres, P. Danesh, 1995, Journal of Non-Crystalline Solids **187**

[32] Goldstein AN 1996 *Appl. Phys. A* **62**, 33-37

[33] M.M. Beerbom, B. Lagel, 2006 Journal of Electron Spectroscopy and Related Phenomena **152**

[34] S. Hüfner, Photoelectron Spectroscopy: Principles and Applications, 2013, Springer Science & Business Media

[35] A. Kahn, 2016, Materials Horizons **1**

[36] Tauc J 1968 *Mater. Res. Bull.* **3**, 37-46

[37] N. F. Mott, E.A. Davis, Electronic Processes in Non-Crystalline Materials, 1971 Clarendon-Press, Oxford

[38] M L Theye, 1989, *Physica Scripta*

[39] N.-M. Park, T.-S. Kim, and S.-J. Park, 2001, Appl. Phys. Lett., **78**, 17

[40] Abdulraheem Y, Gordon I, Bearda T, Meddeb H and Poortmans J, 2014, *AIP Advances* **4**, 057122

[41] A.M. Berntsen and W. F. van der Weg, 1993, *physical review B*

[42] G. D. Cody, T. Tiedje, B. Abeles, B. Brooks, and Y. Goldstein, 1981, *Phys. Rev. Lett.* **47**, 1480

[43] L. Kronik, Y. Shapira, 1999, *Surface Science Reports*, **37**

[44] Carolan D, Rocks C, Padmanaban DB, Maguire P, Svrcek V and Mariotti D 2017, *Sustainable Energy Fuels*, 2017, **1**, 1611-1619

[45] V. Švrček, D. Mariotti, R.A. Blackley, W.Z. Zhou, T. Nagai, K. Matsubara and M. Kondo, 2013, *Nanoscale*, **5**, 6725-6730

[46] M. Bürkle, M. Lozac'h, C. McDonald, D. Mariotti, K. Matsubara, and V. Švrček, 2017, *Adv. Funct. Mater.*, **27**, 1701898